

## STUDY OF THE SPECTRAL AND TEMPORAL CHARACTERISTICS OF X-RAY EMISSION OF THE GAMMA-RAY BINARY LS 5039 WITH *SUZAKU*

TADAYUKI TAKAHASHI<sup>1,2</sup>, TETSUICHI KISHISHITA<sup>1,2</sup>, YASUNOBU UCHIYAMA<sup>3</sup>, TAKAAKI TANAKA<sup>3</sup>, KAZUTAKA YAMAOKA<sup>4</sup>, DMITRY KHANGULYAN<sup>5</sup>, FELIX A. AHARONIAN<sup>5,6</sup>, VALENTI BOSCH-RAMON<sup>5</sup>, JIM A. HINTON<sup>7</sup>

Draft version October 29, 2018

### ABSTRACT

We report on the results from *Suzaku* broadband X-ray observations of the galactic binary source LS 5039. The *Suzaku* data, which have continuous coverage of more than one orbital period, show strong modulation of the X-ray emission at the orbital period of this TeV gamma-ray emitting system. The X-ray emission shows a minimum at orbital phase  $\sim 0.1$ , close to the so-called superior conjunction of the compact object, and a maximum at phase  $\sim 0.7$ , very close to the inferior conjunction of the compact object. The X-ray spectral data up to 70 keV are described by a hard power-law with a phase-dependent photon index which varies within  $\Gamma \simeq 1.45\text{--}1.61$ . The amplitude of the flux variation is a factor of 2.5, but is significantly less than that of the factor  $\sim 8$  variation in the TeV flux. Otherwise the two light curves are similar, but not identical. Although periodic X-ray emission has been found from many galactic binary systems, the *Suzaku* result implies a phenomenon different from the “standard” origin of X-rays related to the emission of the hot accretion plasma formed around the compact companion object. The X-ray radiation of LS 5039 is likely to be linked to very-high-energy electrons which are also responsible for the TeV gamma-ray emission. While the gamma-rays are the result of inverse Compton scattering by electrons on optical stellar photons, X-rays are produced via synchrotron radiation. Yet, while the modulation of the TeV gamma-ray signal can be naturally explained by the photon-photon pair production and anisotropic inverse Compton scattering, the observed modulation of synchrotron X-rays requires an additional process, the most natural one being adiabatic expansion in the radiation production region.

*Subject headings:* acceleration of particles — X-rays: individual (LS 5039) — X-rays: binaries

### 1. INTRODUCTION

LS 5039 is a high-mass X-ray binary (Motch et al. 1997) with extended radio emission (Paredes et al. 2000, 2002). This system is formed by a main sequence O type star and a compact object of disputed nature that has been claimed to be both a black hole (e.g., Casares et al. 2005) and a neutron star/pulsar (e.g., Martocchia et al. 2005; Dubus 2006). The compact object is moving around the companion star in a moderately elliptic orbit (eccentricity  $e = 0.35$ ) with an orbital period of  $P_{\text{orb}} = 3.9060$  days (Casares et al. 2005).

As summarized in Bosch-Ramon et al. (2007), LS 5039 has been observed several times in the X-ray energy band for limited phases in the orbital period. Flux variations on time scale of days and sometimes on much shorter timescales have been reported. The spectrum was always well represented by a power-law model with a photon index ranging  $\Gamma = 1.4\text{--}1.6$  up to  $\sim 10$  keV, with fluxes changing moderately around  $\sim 1 \times 10^{-11}$  erg cm<sup>-2</sup> s<sup>-1</sup>. Softer spectra and larger fluxes had

been also inferred from *RXTE* observations, although background contamination was probably behind these differences (see Bosch-Ramon et al. 2005). Also, *Chandra* data taken in 2002 and 2005 showed spectra significantly harder than 1.5 (Bosch-Ramon et al. 2007), but such a hard spectrum was probably an artifact produced by photon pile-up. Recently, Hoffmann et al. (2009) reported the results of *INTEGRAL* observations in hard X-rays. The source was detected at energies between 25 and 60 keV. The source was detected at energies between 25 and 60 keV. The flux was estimated to be  $(3.54 \pm 2.30) \times 10^{-11}$  erg cm<sup>-2</sup> s<sup>-1</sup> (90 % confidence level) around the inferior conjunction (INFC) of the compact object, and a flux upper limit of  $1.45 \times 10^{-11}$  erg cm<sup>-2</sup> s<sup>-1</sup> (90 % confidence level) was derived at the superior conjunction of the compact object (SUPC).

LS 5039 has also been detected in very-high-energy (VHE:  $E \geq 0.1$  TeV) gamma-rays (Aharonian et al. 2005a), exhibiting a periodic signal modulated with the orbital period (Aharonian et al. 2006). There are two other binary systems with robust detections in the VHE range: PSR B1259–63 (Aharonian et al. 2005b) and LS I +61°303 (Albert et al. 2006; Acciari et al. 2008). Evidence for TeV emission has been found also in Cygnus X-1 (Albert et al. 2007). PSR B1259–63 is a clear case of a high-mass binary system containing a non-accreting pulsar (Johnston et al. 1992), whereas Cygnus X-1 is a well known accreting black hole system (Bolton 1972). The nature of the compact object in LS 5039 is not yet established, and the origin of the VHE emitting electrons is unclear. They may be related to a pulsar wind or to a black hole with a (sub)relativistic jet. In the standard pulsar-wind scenario, the severe photon-photon absorption makes the explanation of the detection of the VHE radia-

Electronic address: takahasi@astro.isas.jaxa.jp

<sup>1</sup> Institute of Space and Astronautical Science/JAXA, 3-1-1 Yoshinodai, Sagamihara, Kanagawa 229-8510, Japan

<sup>2</sup> Department of Physics, University of Tokyo, 7-3-1 Hongo, Bunkyo, Tokyo, 113-0033, Japan

<sup>3</sup> Kavli Institute for Particle Astrophysics and Cosmology, SLAC National Accelerator Laboratory, 2575 Sand Hill Road M/S 29, Menlo Park, CA 94025

<sup>4</sup> Graduate School of Science and Engineering, Aoyama Gakuin University, 5-10-1 Fuchinobe, Sagamihara, Kanagawa 229-8558, Japan

<sup>5</sup> Max-Planck-Institut für Kernphysik, Saupfercheckweg 1, Heidelberg 69117, Germany

<sup>6</sup> Dublin Institute for Advanced Studies, 31 Fitzwilliam Place, Dublin 2, Ireland

<sup>7</sup> School of Physics & Astronomy, University of Leeds, LS2 9JT, Leeds, UK

tion problematic, at least at the position corresponding to the orbital phase  $\phi \sim 0.0$  (see Figs. 16 and 4 from Sierpowska-Bartosik & Torres 2008 and Dubus et al. 2008 and compare with Fig. 5 in Aharonian et al. 2006), in which the emitter is expected to be located between the compact object and the star. However, particles may be accelerated in a relativistic outflow formed at the interaction of the pulsar and the stellar winds (Bogovalov et al. 2008) and radiate far from the compact object, making the pulsar wind scenario a viable option. In the microquasar scenario, the lack of accretion features in the X-ray spectrum may be a problem unless the bulk of the accretion power is released in the form of kinetic energy of the outflow, rather than thermal emission during accretion, as in the case of SS 433 (see e.g., Marshall et al. 2002). At this stage, we cannot give a preference to any of these scenarios, but new data, in particular those obtained with the *Suzaku* satellite, allow us to make an important step towards the understanding of the nature of the non-thermal processes of acceleration and radiation in this mysterious object.

## 2. OBSERVATION

The temporal and spectral characteristics of the X-ray emission from LS 5039 along the orbit should provide important clues for understanding the acceleration/radiation processes in this source. The fact that all previous X-ray observations of this object have incomplete coverage of the orbital period, or suffered from background contamination, is therefore rather unsatisfactory. This motivated our long,  $\sim 200$  ks observation with the *Suzaku* X-ray observatory (Mitsuda et al. 2007), which gives us unprecedented coverage of more than one orbital period, continuously from 2007 September 9 to 15 (see Table 1). *Suzaku* has four sets of X-ray telescopes (Serlemitsos et al. 2007) each with a focal-plane X-ray CCD camera (X-ray Imaging Spectrometer (XIS); Koyama et al. 2007) that are sensitive in the energy range of 0.3–12 keV. Three of the XIS detectors (XIS0, 2 and 3) have front-illuminated (FI) CCDs, whereas XIS1 utilizes a back-illuminated (BI) CCD. The merit of the BI CCD is its improved sensitivity in the soft X-ray energy band below 1 keV. *Suzaku* contains also a non-imaging collimated Hard X-ray Detector (HXD; Takahashi et al. 2007; Kokubun et al. 2007), which covers the 10–600 keV energy band with Si PIN photodiodes (10–70 keV) and GSO scintillation detectors (40–600 keV). *Suzaku* has two default pointing positions, the XIS nominal position and the HXD nominal position. In this observation, we used the HXD nominal position, in which the effective area of HXD is maximized, whereas that of the XIS is reduced to on average  $\sim 88\%$ . Results from XIS2 are not reported here since it has not been in operation since an anomaly in November 2006. In addition, we do not describe in detail the analysis of HXD-GSO data, since the HXD-GSO detected no significant signal from the source.

## 3. DATA REDUCTION

We used data sets processed using the software of the *Suzaku* data processing pipeline (version 2.1.6.16). Reduction and analysis of the data were performed following the standard procedure using the HEADAS v6.4 software package, and spectral fitting was performed with XSPEC v.11.3.2.

For the XIS data analysis, we accumulated cleaned events over good time intervals that were selected by removing spacecraft passages through the South Atlantic Anomaly (SAA). Further, we screened the data with the following criteria — (1) cut-off rigidity is larger than 6 GV and (2) elevation

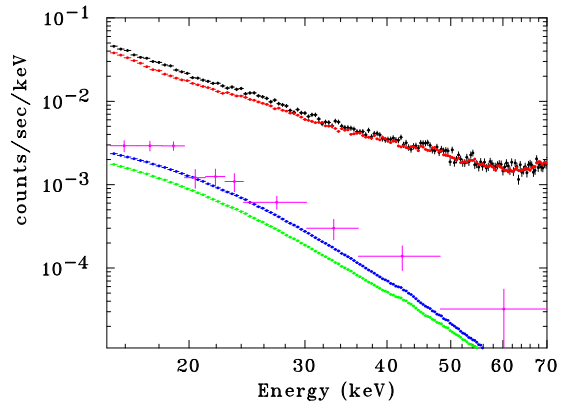


FIG. 1.— The HXD-PIN spectrum. The black, red, blue, green, and magenta points show the count rates based on the raw data, from the modeling of NXB, the CXB component, the GRXE component, and the background-subtracted data, respectively. The background here includes contributions from the NXB, CXB and GRXE (see §2 for details).

angle from the Earth’s rim is larger than  $5^\circ$ . The source photons were accumulated from a circular region with a radius of  $3'$ . The background region was chosen in the same field of view with the same radius and an offset of  $9'$  from the source region. We have co-added the data from the two FI-CCDs (XIS0 and XIS3) to increase statistics. The response (RMF) files and the auxiliary response (ARF) files used in this paper were produced using `xisrmfgen` and `xissimarfgen`, respectively.

For the HXD data, “uncleaned event files” were screened with the standard event screening criteria: the cut-off rigidity is larger than 6 GV, the elapsed time after the passage of the SAA is more than 500 s and the time to the next SAA passage is more than 180 s, high voltages from all eight HV units are within the normal range and the elevation angle from the Earth’s rim is more than  $5^\circ$ . We also discarded telemetry-saturated time intervals. In the spectral analysis in §3, we used the response file for a point-like source at the HXD-nominal position (`ae_hxd_pinhxnome4_20070914.rsp`), which is released as a part of CALDB (*Suzaku* calibration data base).

The HXD-PIN spectrum is dominated by the time-variable instrumental background (non-X-ray background (NXB)) induced by cosmic rays and trapped charged particles in the satellite orbit. To estimate the instrumental background component, we used the time-dependent NXB event files released by the HXD instrument team, whose reproducibility is reported by Fukazawa et al. (2009). In order to estimate the systematic uncertainty of the NXB model during our observation, we compare the NXB model spectrum during Earth occultation with the observed spectrum of the same time interval. The event selection criteria for this study are the same as those of the cleaned event except for the criterion on Earth elevation angle, which was chosen to be less than  $-5^\circ$ . The estimated uncertainty obtained is  $\sim 3\%$ , which is consistent with the values reported by Fukazawa et al. (2009).

Another component of the HXD-PIN background is the cosmic X-ray background (CXB). In our analysis, we assumed the CXB spectrum reported by (Gruber et al. 1999):

$$I(\epsilon) = 7.9 \epsilon_{\text{keV}}^{-1.29} \exp\left(-\frac{\epsilon_{\text{keV}}}{\epsilon_p}\right) \text{ ph s}^{-1} \text{ keV}^{-1} \text{ cm}^{-2} \text{ str}^{-1}, \quad (1)$$

where  $\epsilon_{\text{keV}} = \epsilon/\text{keV}$  and  $\epsilon_p = 41.1$ . The CXB spectrum observed with HXD-PIN was simulated by us

TABLE 1  
LOG OF *Suzaku* OBSERVATIONS

Obs. ID	Coord. (J2000) RA, DEC	Exposure XIS/HXD	Date
402015010	18 <sup>h</sup> 26 <sup>m</sup> 15 <sup>s</sup> .1, -14 <sup>d</sup> 50 <sup>m</sup> 54 <sup>s</sup> .2	203 ks/181 ks	09–15/09/2007

Note.—The exposure time is the net integration time after standard data screening for the XIS and HXD-PIN.

ing a PIN response file for isotropic diffuse emission (`ae_hxd_pinflate4_20070914.rsp`) and added to the NXB spectrum. Based on this approach, the contribution from the CXB flux is  $\sim 5\%$  of the NXB.

Since LS 5039 is located close to the Galactic plane, the contribution from the Galactic ridge X-ray emission (GRXE) must be examined, especially for HXD-PIN spectra. In order to model the shape of the GRXE, data from *Suzaku* observations of the Galactic ridge region (ObsID: 500009010 and 500009020) were analyzed. The *Suzaku* spectrum from 3 keV to 50 keV can be well fitted with the Raymond-Smith plasma with a temperature of  $kT = 2.2 \pm 0.8$  keV and a power-law function with  $\Gamma = 1.92^{+0.28}_{-0.4}$ . Although we also tried a power law with exponential cutoff, following the results from the *INTEGRAL* IBIS (Krivonos et al. 2007), it turned out that the assumption on the spectral shape of the GRXE has negligible effect on the spectral parameters of LS 5039. The normalization of the GRXE spectrum component in the HXD-PIN spectrum of LS 5039 is determined from the XIS spectrum of the LS 5039 observation by excluding an encircled region with a radius of  $4.5'$  centered on the LS 5039 location. The flux of the GRXE is estimated to be  $\sim 40\%$  of the contribution from the CXB. In Figure 1, we show the time averaged HXD-PIN spectrum plotted together with models for the NXB, CXB and GRXE.

#### 4. ANALYSIS AND RESULTS

##### 4.1. Temporal analysis

The light curve obtained from the XIS detector is shown in the top panel of Figure 2. The continuous coverage in X-rays, longer than the orbital period of the LS 5039 system, reveals a smooth variation of a factor 2 in the 1–10 keV count rate. The light curve is drawn over two orbital periods. The orbital phase is calculated with the period of 3.90603 days, and  $\phi = 0$  with reference epoch  $T_0$  (HJD–2400000.5 = 51942.59) taken from Casares et al. (2005). The light curve from phase  $\phi = 1.0$  to 1.5, which was obtained in the last part of the observation, smoothly overlaps with the one obtained at the beginning of the observation ( $\phi = 0.0$ –0.5).

In the middle panel of Figure 2, we present the light curve obtained with the HXD-PIN for the energy range 15–40 keV. Although the statistical errors are larger, the modulation behavior is similar to that of the XIS. The amplitude of the modulation is roughly the same between the XIS and HXD-PIN, indicating small changes of spectral shape depending on orbital phase. The spectral parameters obtained for each orbital phase are reported in the following section.

The light curves obtained with *Suzaku* show that the X-ray flux minimum appears around phase 0.0–0.3 and it reaches maximum around phase 0.5–0.8. In order to quantify the amplitude of the flux variations, we fitted the XIS light curve with a simple sinusoidal function. Due to structures in the light curve, the fit converges with large chi-square ( $\chi^2_\nu(\nu) = 4.92$  (121)). However, the general trend is well represented

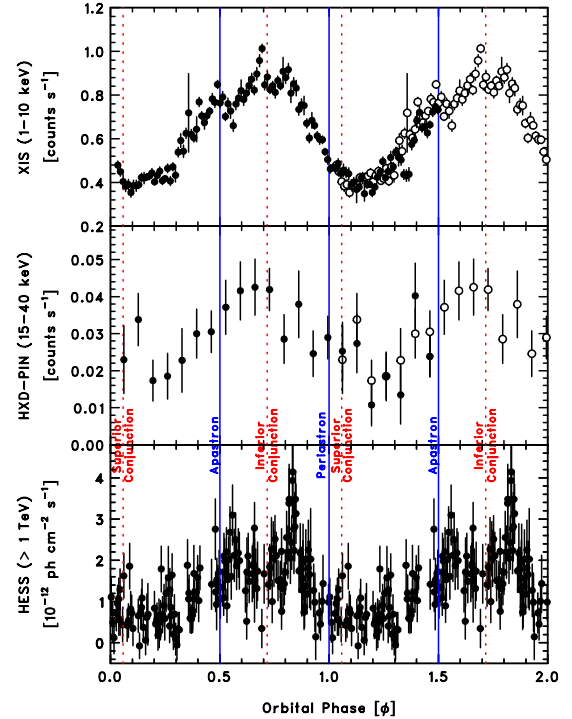


FIG. 2.— Orbital light curves observed for LS 5039. (Top) *Suzaku* XIS count rate in the 1–10 keV band continuously obtained for a 200 ks duration (filled circles), which covers one orbit and a half. Overlaid is the same light curve but shifted by one orbital period (open circles). (Middle) *Suzaku* PIN count rate in the 15–40 keV band. Background components consisting of NXB, CXB and GRXE are subtracted. (Bottom) the light curve of integral fluxes at energies  $E > 1$  TeV vs. orbital phase ( $\phi$ ) obtained on run-by-run basis from the HESS data (2004 to 2005) reported by Aharonian et al. (2006).

by a sinusoidal function:

$$I(\phi) = 0.24 \sin(\phi - 0.13) + 0.64 \text{ counts s}^{-1} \quad (2)$$

where  $I(\phi)$  is the count rate as a function of phase  $\phi$ . The ratios between the minimum and maximum count rates are  $2.21^{+0.02}_{-0.03}$  counts  $\text{s}^{-1}$  for XIS and  $2.02^{+0.25}_{-0.19}$  counts  $\text{s}^{-1}$  for HXD-PIN. Structures of the X-ray and hard X-ray light curves are similar to that discovered in the phase diagram of integral fluxes at energies  $> 1$  TeV obtained on a run-by-run basis from HESS data (2004 to 2005) (Aharonian et al. 2006). The temporal X-ray behavior was already suggested by *RXTE* data, as well as by a compilation of all the previous X-ray data obtained with imaging instruments (Bosch-Ramon et al. 2005; Zabalza et al. 2008).

In addition to the continuously changing component with respect to the orbital phase, short timescale structures are found around  $\phi = 0.48$  and  $\phi = 0.7$ . The unabsorbed flux changes about a 30% in  $\Delta\phi \sim 0.05$  ( $= 4.7$  hour). A significant dip can be seen around  $\phi = 1.35$  in the top panel of Figure 2. In comparison with the data at around  $\phi = 0.35$  obtained in the first half of the observation, the flux decreased  $\sim 50\%$  only

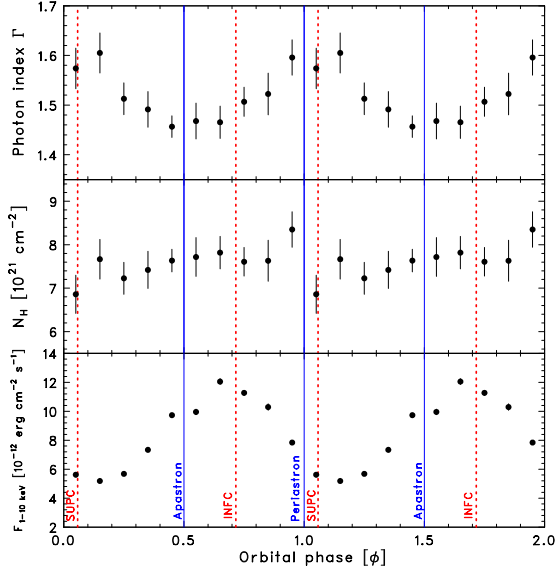


FIG. 3.— Orbital light curves of the photon indices,  $N_H$ , and unabsorbed fluxes in the energy range of 1–10 keV obtained by fitting with an absorbed power-law model. The phase interval width is  $\Delta\phi = 0.1$ . Two full phase periods are shown for clarity. The blue solid lines show periastron and apastron phase and red dashed lines show SUPC and INFC of the compact object.

in this phase. The time duration of this dip corresponds to  $\Delta\phi \sim 0.03$ . These structures may reflect features of the (possibly changing) environment of the X-ray emitting region, it is therefore of importance to test with further observations if these are persistent features.

#### 4.2. Spectral Analysis

Firstly we study time-resolved (phase-resolved) X-ray spectra. The data are divided into data segments with respect to the assigned phase, and model fitting is performed for XIS spectra for each segment with  $\Delta\phi = 0.1$ .

A single power-law function with photoelectric absorption, provides a good fit for all the segments. In order to study the possible changes of the amount of photoelectric absorption, we here fit the data with  $N_H$  free. The best-fit parameters are presented in Table 2. The derived values of the photon index and absorption column density are consistent with previous observations (Martocchia et al. 2005; Bosch-Ramon et al. 2007). When we fix the  $N_H$  to the value obtained from the time averaged spectrum, resultant photon indices stay same within statistical error.

The photon index ( $\Gamma$ ) values are plotted as a function of orbital phase in the top panel of Figure 3. The spectral shape varied such that the spectrum is steep around SUPC ( $\Gamma \simeq 1.61$ ) and becomes hard ( $\Gamma \simeq 1.45$ ) around apastron. The modulation behavior of  $\Gamma$  is somewhat different from that observed using HESS in the VHE range. The amplitude of the variation is  $\pm 0.1$ , which is much smaller than the change of  $\pm 0.6$  in the VHE region (Aharonian et al. 2006). The 1–10 keV flux changes from  $(5.18 \pm 0.03) \times 10^{-12} \text{ erg cm}^{-2} \text{ s}^{-1}$  ( $\phi = 0.1\text{--}0.2$ ) to  $(12.05 \pm 0.02) \times 10^{-12} \text{ erg cm}^{-2} \text{ s}^{-1}$ . ( $\phi = 0.6\text{--}0.7$ ).

In all the data segments, the source is significantly detected with the HXD-PIN, indicating that hard X-ray emission extends at least up to 70 keV. Note also that although the XIS and HXD-PIN spectra do not overlap, they seem to be smoothly connected in the gap between 10 and 15 keV.

To study the shape of the spectrum above 10 keV, the XIS spectra and the PIN spectrum in the range 15–70 keV after

subtraction of background (NXB + CXB + GRXE) are jointly fitted (Figure 4 Top). The time-averaged spectra are well represented by an absorbed power-law model with  $\Gamma = 1.51 \pm 0.02$  with reduced  $\chi^2_{\nu} = 0.99$  (235 degrees of freedom). We find no cutoff structure in the energy range of the HXD-PIN. The spectra within the phase intervals  $[0.616 < \phi < 0.816]$  and  $[\phi < 0.158 \text{ \& } 0.958 < \phi]$ , which correspond to the INFC and SUPC, respectively, are also shown in Figure 4. The best-fit parameters are presented in Table 3.

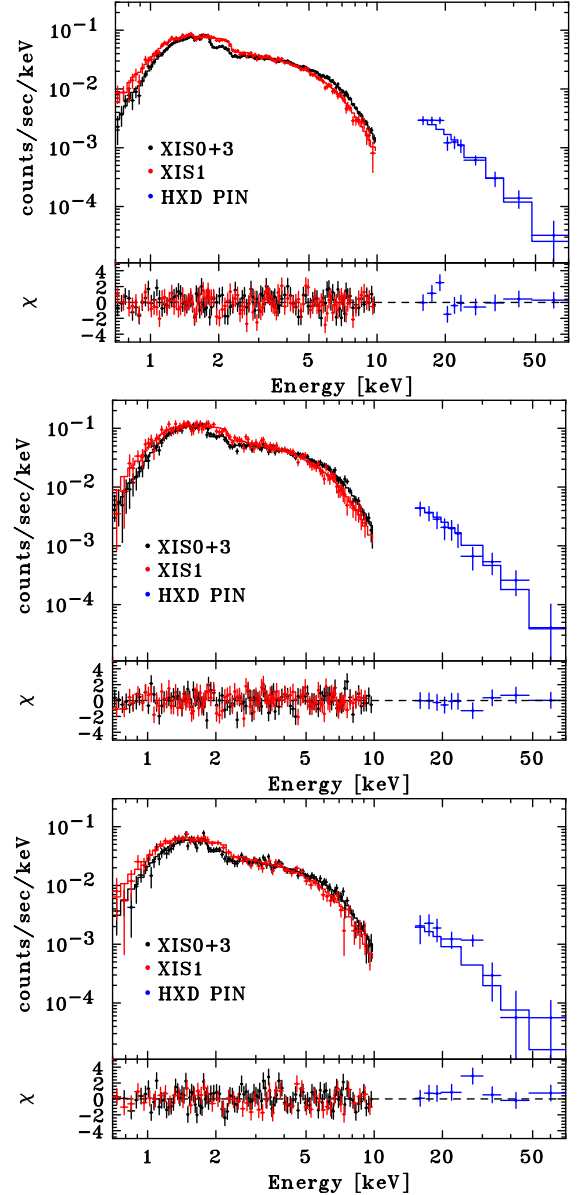


FIG. 4.— Top: The time-averaged *Suzaku* (XIS+HXD) spectrum (Top) and spectra obtained in INFC (Middle) and SUPC (Bottom).

Although earlier observations by *RXTE* suggested the presence of an iron emission line at 6.7 keV (Ribo et al. 1999), later observations by *Chandra* and *XMM* could not find evidence of it (e.g. Bosch-Ramon et al. 2005). A careful study of new and longer *RXTE* observations, using slew data to account for background emission, revealed that the earlier reported 6.7 keV emission line is likely a background feature

TABLE 2  
RESULTS OF *Suzaku* XIS SPECTRAL FITTING

Orbital Phase Intervals	Photon index	$N_H$ ( <i>wabs</i> ) $10^{21} \text{ cm}^{-2}$	Flux [1-10 keV] $10^{-12} \text{ erg cm}^{-2} \text{ s}^{-1}$	$\chi^2_\nu(\nu)$
INFC ( $0.45 < \phi \leq 0.9$ )	$1.48 \pm 0.02$	$7.82 \pm 0.18$	$10.78 \pm 0.05$	0.97 (111)
SUPC ( $\phi \leq 0.45, 0.9 < \phi$ )	$1.55 \pm 0.02$	$7.77 \pm 0.20$	$6.72 \pm 0.04$	0.94 (111)
All Phases (time averaged)	$1.51 \pm 0.01$	$7.71 \pm 0.2$	$8.07 \pm 0.03$	0.81 (118)
0.0-0.1	$1.57 \pm 0.04$	$6.86 \pm 0.44$	$5.62 \pm 0.03$	0.99 (111)
0.1-0.2	$1.61 \pm 0.04$	$7.67 \pm 0.46$	$5.18 \pm 0.03$	1.04 (111)
0.2-0.3	$1.51 \pm 0.03$	$7.23 \pm 0.37$	$5.67 \pm 0.02$	1.13 (107)
0.3-0.4	$1.49 \pm 0.03$	$7.42 \pm 0.43$	$7.34 \pm 0.03$	1.01 (111)
0.4-0.5	$1.45 \pm 0.02$	$7.63 \pm 0.26$	$9.73 \pm 0.01$	0.96 (111)
0.5-0.6	$1.46 \pm 0.03$	$7.72 \pm 0.45$	$9.95 \pm 0.02$	1.15 (105)
0.6-0.7	$1.46 \pm 0.03$	$7.82 \pm 0.37$	$12.05 \pm 0.02$	0.77 (118)
0.7-0.8	$1.51 \pm 0.02$	$7.61 \pm 0.33$	$11.27 \pm 0.02$	1.10 (108)
0.8-0.9	$1.52 \pm 0.04$	$7.63 \pm 0.47$	$10.29 \pm 0.03$	0.87 (111)
0.9-1.0	$1.59 \pm 0.03$	$8.35 \pm 0.41$	$7.84 \pm 0.02$	1.06 (111)

Note.—Fitting *Suzaku* XIS0 +XIS3 spectrum of LS5039 by a power-law with photoelectric absorption in 0.6–10 keV. Photon index  $\Gamma$ , absorbing column density  $N_H$ , and the 1–10 keV flux  $F_{1-10}$  (corrected for absorption) are shown with 68.3 % ( $1 \sigma$ ) error. The orbital phase  $\phi$  is calculated from the ephemeris of Casares et al. (2005).

TABLE 3  
RESULTS OF LS 5039 XIS+HXD-PIN SPECTRAL FITTING

Orbital Phase Intervals	Photon index	$N_H$ ( <i>wabs</i> ) $\times 10^{21} \text{ cm}^2$	$\chi^2_\mu(\nu)$
All Phases (time averaged)	$1.51 \pm 0.02$	$7.7 \pm 0.2$	0.95 (175 d.o.f.)
INFC ( $0.616 < \phi < 0.816$ )	$1.49 \pm 0.04$	$7.9 \pm 0.4$	0.87
SUPC ( $\phi < 0.158, 0.958 < \phi < 1.158$ )	$1.55 \pm 0.05$	$6.9 \pm 0.5$	1.06

Note.—Power-law fitting to the XIS/HXD-PIN spectrum. The errors of spectral parameters are at the 90% confidence level.

(Bosch-Ramon et al. 2005). The *Suzaku* data confirm this result. In an attempt to find the possible signature of iron emission lines from LS 5039, we analyzed the phase-averaged spectrum. The upper limits on iron line structures are determined by fitting a Gaussian at various energies and line widths at which Fe emission might be expected. The power-law continuum model parameters are fixed with the best fit values and a Gaussian component is added to the power-law function. The central energy of the Gaussian line is swept from 6.0 keV to 7.1 keV in steps of 0.1 keV. Line widths are changed from 0.01 keV to 0.09 keV in steps of 0.01 keV, together with lines with larger widths of 0.15 and 0.20 keV. An equivalent width is determined at each grid point. The resulting upper-limit on the equivalent width is 40 eV with 90% confidence level.

## 5. DISCUSSION

The X-ray emission observed with *Suzaku* is characterized by (1) a hard power law with  $\Gamma \simeq 1.5$  extending from soft X-rays to  $\sim 70$  keV, (2) clear orbital modulation in flux and photon index, (3) a moderate X-ray luminosity of  $L_X \sim 10^{33} (\frac{d}{1 \text{ kpc}})^2 \text{ erg s}^{-1}$ , (4) a small and constant absorbing column density, and (5) a lack of detectable emission lines.

Although variable X-ray emission has been found from more than two hundred galactic binary systems, the *Suzaku* data hardly can be explained within the “standard accretion” scenario where X-rays are produced by a hot thermal (comptonized) accretion plasma around the compact object. The lack of X-ray emission lines (at the level of sensitivity of *Suzaku*) as well as the hard  $E^{-1.5}$  type energy spectrum of the X-ray continuum, extending from soft X-rays up to 70 keV,

favors a non-thermal origin of the X-rays. This conclusion is supported by the general similarities between the properties of the observed X-rays and TeV gamma-rays. Namely, both radiation components require a rather hard energy distribution of parent electrons with a power-law index of  $\approx 2$ . This directly follows from the photon index of the synchrotron radiation  $\Gamma \approx 1.5$ , and agrees quite well with the currently most favored interpretation of the TeV gamma-rays, in which they would be produced by IC scattering off the anisotropic photon field of the massive companion star.

Assuming that the TeV gamma-ray production region is located at a distance from the companion star of  $d \sim 2 \times 10^{12} \text{ cm}$  (i.e. the binary system size), and taking into account that gamma-rays are produced in the deep Klein-Nishina (KN) regime with significantly suppressed cross-section, for the well known luminosity of the optical star  $L \simeq 7 \times 10^{38} \text{ erg s}^{-1}$ , one can estimate quite robustly the strength of the magnetic field in the emission region. The numerical calculations show that the field should be around a few Gauss (see e.g. Fig. 5). For such a magnetic field strength, the energy intervals of electrons responsible for the two emission components overlap substantially, as shown in Figure 5. Therefore, we are most likely dealing with the same population of parent electrons, which should be located at large distances from the compact object, in the system periphery, to prevent the severe absorption of the TeV radiation and the subsequent intense emission from the pair-created secondaries (Khagulyan et al. 2008a; Bosch-Ramon et al. 2008a).

It should be noted that the observed X-ray emission is very difficult to explain as synchrotron emission produced by sec-

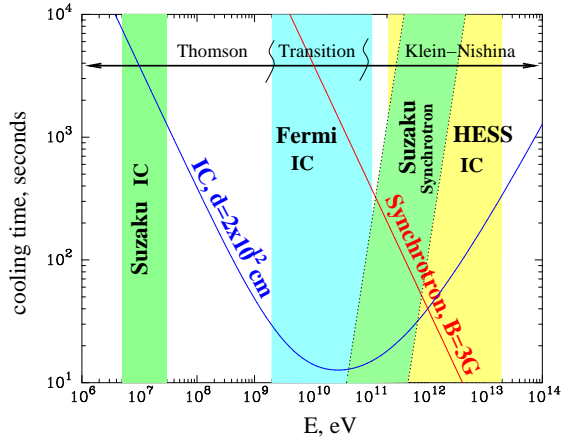


FIG. 5.— The radiative cooling times as a function of electron energy. The blue line corresponds to IC losses at the distance  $d = 2 \times 10^{12}$  cm from the optical star (the star luminously and temperature were assumed to be  $L_* = 7 \times 10^{38}$  erg/s and  $T_* = 3.8 \times 10^4$  K, respectively). The red line corresponds to the synchrotron losses for B-field  $B = 3$  G. The filled regions reproduce the electron energy intervals relevant to the HESS (yellow), *Fermi* (light blue) and *Suzaku* (green) energy domains. Formally, two radiation channels, synchrotron radiation of very high energy electrons (light green) and IC scattering of low energy electrons in the Thomson regime (dark green) can produce X-ray photons in the *Suzaku* energy domain.

ondary (pair-produced) electron and positrons. Since the pair production cross-section has strong energy dependence with a distinct maximum, for the target photons of typical energy of  $\sim 10$  eV, the major fraction of the absorbed energy will be released in the form of  $\sim 100$  GeV electrons. Thus secondary pair synchrotron emission must show a spectral break in the *Suzaku* energy band unless one assumes unreasonably high magnetic fields,  $B \geq 1$  kG, in the surroundings of the gamma-ray emission region (Khangulyan et al. 2008a; Bosch-Ramon et al. 2008a).

Figure 5 shows the synchrotron and IC cooling times of electrons, as a function of electron energy, calculated for the stellar photon density at  $d = 2 \times 10^{12}$  cm and for a magnetic field  $B = 3$  G. It can be seen that synchrotron losses dominate over IC losses at  $E_e \geq 1$  TeV. Note that the TeV gamma-ray production takes place in the deep KN regime. This implies that the cooling time,  $t_{\text{cool}} = \gamma/\dot{\gamma}$ , of electrons generating GeV gamma-rays via IC scattering (Thomson regime) is shorter than the cooling time of TeV electrons responsible for producing very high-energy gamma-rays (KN). The same applies for synchrotron cooling time of multi-TeV electrons that produce low-energy (MeV) gamma-rays by synchrotron radiation. One should therefore expect significantly higher MeV (synchrotron) and GeV (IC) fluxes than at keV and TeV energies, provided that the acceleration spectrum of electrons extends from low energies to very high energies. However, in the case of existence of low-energy and very-high-energy cutoffs in the acceleration spectrum, the gamma-ray fluxes  $> 10$  MeV and at GeV energies would be significantly suppressed.

To better understand the energy ranges of the electrons responsible for X-ray and gamma-ray production, we show in Figure 5 the energy zones of electrons relevant to the *Suzaku*, *Fermi*, and HESS radiation domains. Note that the reconstruction of the average energy of electrons responsible for the IC gamma-rays depends only on the well known temperature of the companion star  $T = 3.8 \times 10^4$  K. The light green zone in Figure 5 marked as “*Suzaku* synchrotron”, corresponds to

electrons responsible for the synchrotron photons produced in the energy interval  $1 \text{ keV} \leq \epsilon_{\text{syn}} \leq 40 \text{ keV}$ . For a reasonable range of magnetic field values, the energy interval of electrons relevant for *Suzaku* data overlap on one hand with the HESS energy interval, and can overlap with the *Fermi* one. This should allow us, in the case of detection of MeV/GeV gamma-rays by *Fermi*, to considerably reduce the parameter space, in particular, to better localize the X- and gamma-ray production regions from electromagnetic cascade constraints, and derive the broadband energy spectrum of electrons and the strength of the magnetic field, both as a function of the orbital phase.

Formally, when X-rays and TeV gamma-rays are produced by the same population of very-high-energy electrons, one should expect a general correlation between the light curves obtained by *Suzaku* and HESS. In this regard, the similarity between the *Suzaku* and HESS light curves seems to be natural. However, such an interpretation is not straightforward in the sense that two major mechanisms that might cause modulation of the TeV gamma-ray signal are related to interactions of electrons and gamma-rays with the photons of the companion star, i.e. anisotropic IC scattering and photon-photon pair production (Khangulyan et al. 2008a; Dubus et al. 2008), and thus cannot contribute to the X-ray modulation. The X-ray modulation requires periodic changes of the strength of the ambient magnetic field or the number of relativistic electrons. Note, however, that the change of magnetic field would not have a strong impact as long as the radiation proceeds in the saturation regime and synchrotron losses dominate in the relevant energy interval. One would also expect modulation of the synchrotron X-ray flux if the energy losses of electrons are dominated by IC scattering, although in such a case we should observe significantly lower X-ray fluxes.

A more natural reason for the modulation of the synchrotron fluxes would come from dominantly adiabatic losses. The adiabatic cooling of electrons in binary systems can be realized through complex (magneto)hydrodynamical processes, e.g. due to interactions between a black hole jet or a pulsar wind with the dense stellar wind of a massive companion star (see e.g. Bogovalov et al. 2008, Perucho & Bosch-Ramon 2008). The orbital motion could naturally produce the modulation of adiabatic cooling of electrons around the orbit (see e.g. Khangulyan et al. 2008b). Note that because of the relatively small variation of the X-ray flux over the orbit, a factor of only two, the requirements for this scenario are quite modest. We note that dominant adiabatic losses have been invoked by Khangulyan et al. (2007) to explain the variations of the X-ray and TeV gamma-ray fluxes from the binary pulsar PSR B1259–63.

The detected power-law spectrum of X-rays with photon index around  $\Gamma = 1.5$  implies that the established energy spectrum of electrons is also a power-law with index  $\alpha_e \simeq 2$ . This agrees well with the hypothesis of dominance of adiabatic losses, because the adiabatic losses do not change the initial spectrum of electrons. Thus the required power-law index  $\alpha_e \simeq 2$  implies a reasonable acceleration spectrum  $Q(E_e) \propto E_e^{-2}$ . Otherwise, in an environment dominated by synchrotron losses, the acceleration spectrum should be very hard, with a power-law index  $\leq 1$ , or should have an unreasonably large low-energy cutoff at  $E \geq 1$  TeV to explain the observed X-ray spectra.

Obviously, adiabatic losses modulate the IC gamma-ray

flux in a similar manner. However, unlike X-rays, the TeV gamma-rays suffer significant distortion due to photon-photon absorption (see e.g. Böttcher 2007) and anisotropic IC scattering with its strong hardening of the gamma-ray spectrum (Khangulyan & Aharonian 2005). All this leads to additional orbital modulation of the gamma-ray signal, and it is likely that these two additional processes are responsible for the strong change of gamma-ray flux, much more pronounced than that seen in X-rays (see Fig. 2). The *Suzaku* data presented in this paper implies a key additional assumption, namely that the accelerated electrons must lose their energy adiabatically before they cool radiatively.

In order to demonstrate that the suggested scenario can satisfactorily explain the combined *Suzaku* X-ray and HESS gamma-ray data, we performed calculations of the broad-band spectral energy distributions (SEDs) of the synchrotron and IC emission, assuming a simple model in which the same population of electrons is responsible for both X-rays and TeV gamma-rays. We also assumed that the emission region has homogeneous physical conditions. This is a reasonable assumption given that we deal with very short cooling timescales ( $\ll 100$  s), thus electrons cannot travel significant distances while emitting.

In the regime dominated by adiabatic energy losses, the synchrotron X-ray flux is proportional to  $t_{\text{ad}}$ . The X-ray modulation seen by *Suzaku* is then described by the modulation of the adiabatic loss rate. In Fig. 6, we show  $t_{\text{ad}}(\phi)$  that is inferred from the X-ray data. The required adiabatic cooling timescales are  $\sim 1$  s. Any consistent calculation of the adiabatic cooling requires the solution of the corresponding hydrodynamical problem, and one needs to know in detail the nature of the source. At the present stage, we consider the simple example of adiabatic cooling in a relativistically expanding source. In such a case, the adiabatic loss rate can be written as:  $\dot{\gamma}_{\text{ad}}(\phi, \gamma) = \gamma/t_{\text{ad}}$  with  $t_{\text{ad}} \sim R/c \simeq 3R_{11}$  sec, where  $R_{11} \equiv R/(10^{11} \text{ cm})$  is the characteristic size of the source. The required variation of the adiabatic cooling is thus reduced to the modulation of the size of the radiation region ( $R_{11} \sim 0.3-1$ ). The size in turn depends on the external pressure exerted by, e.g., the stellar wind from the massive star. The expected weaker external pressure around apastron implicitly assumed in our model would be broadly consistent with the radial dependence of the wind pressure.

In Fig. 7 we show the SEDs averaged over the INFC ( $\phi = 0.45-0.9$ ) and SUPC ( $\phi \leq 0.45, \phi \geq 0.9$ ) phase intervals. The corresponding gamma-ray data have been previously reported by HESS (Aharonian et al. 2006). Since both the absolute flux and the energy spectrum of TeV gamma-rays vary rapidly with phase, in order to compare the theoretical predictions with observations, we should use smaller phase bins, ideally speaking with the time intervals  $\Delta t \leq 100$  s corresponding to the characteristic cooling timescales of electrons. Because of the lack of the relevant gamma-ray data available to us, we here use the X-ray and gamma-ray data integrated over  $\Delta\phi = 0.45$ . While this compromise does not allow us to perform quantitative studies, it can be used to make a qualitative comparison of the model calculations with observational data.

The theoretical calculations of the SEDs are in a reasonable agreement with the observed spectra, though they do not perfectly match the gamma-ray fluxes. One can improve the fits by introducing slight phase-dependent changes in the spectra of accelerated electrons, but it is beyond the scope of this paper given the caveat mentioned above. We should also note

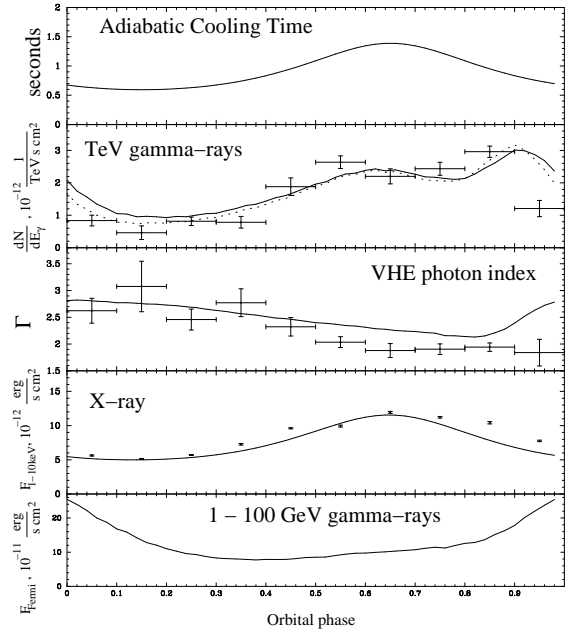


FIG. 6.— Lightcurves. (a) the phase dependence of adiabatic losses derived from the *Suzaku* data; (b) solid line: calculated 1 TeV gamma-ray fluxes together with HESS data points, dotted line: the normalizations at 1 TeV of power-law fits for the calculated spectra; (c) calculated photon indices around 1 TeV together with power-law indices reported by HESS; (d) calculated 1–10 keV X-ray fluxes with the reported *Suzaku* data; and (e) predicted 1–100 GeV integrated IC flux (note that the peak in the spectrum is at 10 GeV; see Fig. 7). The calculations were performed for the following parameters: inclination of the orbit  $i = 30$  deg; elevation over the orbital plane  $Z_0 = 1.8 \times 10^{12}$  cm; magnetic field strength  $B = 2.5$  G. A power-law injection spectrum of electrons  $Q(E) \propto E_e^{-2}$  ( $10 \text{ GeV} < E_e < 100 \text{ TeV}$ ) was assumed. The total power injected in relativistic electrons was fixed at the level of  $10^{37}$  erg/s. The cooled electron spectrum is formed due to radiative (IC and synchrotron) and non-radiative (adiabatic) losses, derived from the *Suzaku* data.

that the calculations of low energy gamma-rays (in the *Fermi* domain) are performed assuming that the injection spectrum of electrons continues down to 10 GeV. If this is not the case, the gamma-ray fluxes in the *Fermi* energy domain may be significantly suppressed. On the other hand, the detection of gamma-rays by *Fermi* would allow us to recover the spectrum of electrons in a very broad energy interval, and thus distinguish between different acceleration models. Another important feature in this scenario is that a hard synchrotron spectrum extending up to a few MeV, is required by the robust detection of  $\sim 10$  TeV gamma-rays from the system. A future detection of the emission at MeV energies may bring important information on the presence of highest energy particles in the system.

The reproduction, at least qualitatively, of the observed spectral and temporal features of the nonthermal radiation with the simple toy model supports the production of X-ray and TeV gamma-rays by the same population of parent particles and allows us to derive several principal conclusions. The electron energy distribution should be a power-law with an almost constant index of  $\alpha_e = 2\Gamma_X - 1 \simeq 2$  to explain the X-ray spectra. Note that in an *isotropic* photon gas when the Compton scattering takes place in the deep KN regime such an electron distribution results in a quite steep TeV spectrum with photon index  $\Gamma_\gamma \simeq 1 + \alpha_e \simeq 3$ . This does not agree with HESS observations. However, the anisotropic IC provides a remarkable hardening of the gamma-ray spectrum (Khangulyan & Aharonian 2005), in particular,  $\Gamma_\gamma \sim 2$  would

be expected for the INFC, and it has indeed been observed using HESS (Aharonian et al. 2006). We also note that, to explain the VHE spectrum at SUPC, we have to assume that the emission region is located at a distance  $\approx 2 \times 10^{12}$  cm from the compact object, in the direction perpendicular to the orbital plane. In the standard pulsar scenario, the production region cannot be located far away from the compact object, and even invoking electromagnetic cascading (see e.g. Fig. 16 in Torres & Sierpowska-Bartosik 2008), one cannot reproduce the reported fluxes around orbital phase 0.0 (Khangulyan et al. 2008a; Bosch-Ramon et al. 2008a). We have found that the magnetic field strength cannot deviate much from a few G. We can also derive a constraint on the size of the emission region, imposing a maximum expansion speed of  $\sim c$  (the speed of light), and the Hillas criterion (Hillas 1984), in which the minimum size of a source capable of accelerating particles to a given energy  $E_e$  is  $R = R_L$  (where  $R_L = E_{eV}/300B_G$  cm), the Larmor radius. This estimate yields a size of  $10^{10}$ – $10^{11}$  cm, which agrees quite well with the estimate based on the required timescale of adiabatic cooling. Note that the requirement of fast adiabatic losses imposes a strong constraint on the acceleration rate of electrons. Indeed, the acceleration timescale can be expressed as:  $t_{\text{acc}} = \eta R_L/c \sim 0.1\eta(E_e/1\text{TeV})(B/1\text{G})^{-1}$  s, where  $\eta \geq 1$  parametrizes the acceleration efficiency. In extreme accelerators with the maximum possible rate allowed by classical electrodynamics  $\eta = 1$ . The HESS spectrum provides evidence of electron acceleration well above 10 TeV. Therefore,  $t_{\text{acc}} < t_{\text{ad}} \sim 1$  s is required at  $E_e = 10$  TeV, which translates into  $\eta < 3$  for  $B = 3$  G. Thus we arrive at the conclusion that an extremely efficient acceleration with  $\eta < 3$  should operate in a compact region of  $R \sim 10^{11}$  cm.

Finally, we would like to emphasize that in the scenario described here different radiation energy intervals are characterized by fundamentally different light curves. While the synchrotron X-ray modulation is caused by adiabatic losses, the light curve in gamma-rays depends critically, in addition, on effects related to interactions with the optical photons of the companion star. Two of these effects, photon-photon pair production and anisotropic Compton scattering are equally important for the formation of the light curve of TeV gamma-rays. On the other hand, only the effect of anisotropic Compton scattering has an impact on the formation of the light curve of GeV gamma-rays. The difference of light curves in the X-ray and GeV and TeV gamma-ray intervals in this scenario is shown in Figure 6.

## 6. SUMMARY

The *Suzaku* X-ray satellite has observed LS 5039 for the first time with imaging capabilities over one and a half orbits. The *Suzaku* data show strong modulation of the X-ray emission at the orbital period of the system and the X-ray spectral data are described by a hard power-law up to 70 keV. We found the close correlation of the X-ray and TeV gamma-ray light curves, which can be interpreted as evidence of production of these two radiation components by the same electron population via synchrotron radiation and IC scattering, respectively. Whereas there are at least two reasons for the formation of a periodic TeV gamma-ray light curve, both related to the interaction with photons from the companion star (photon-photon absorption of VHE gamma-rays and IC scattering in an anisotropic photon field), the modulated X-ray

signal requires an additional effect. A simple and natural re-

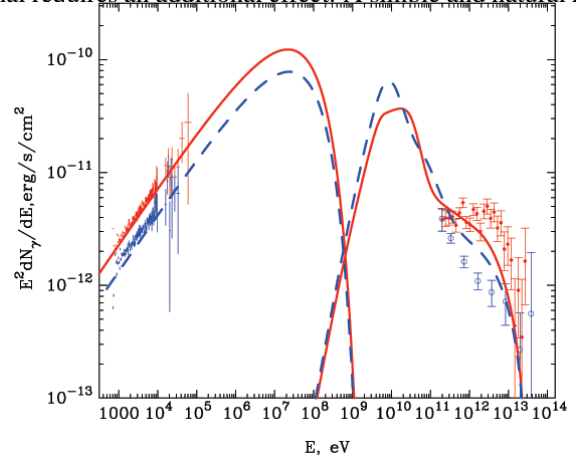


FIG. 7.— Model calculations of the non-thermal radiation spectra of LS 5039, averaged over SUPC (low state) and INFC (high state) orbital phase intervals for  $\phi \leq 0.45$ ,  $\phi \geq 0.9$  (SUPC, Blue); and for  $\phi = 0.45$ – $0.9$  (INFC, Red). The flux points of *Suzaku* X-ray spectra (1–40 keV band) are reconstructed with the best-fit function with correction for the interstellar absorption. The HESS gamma-ray spectra are taken from Aharonian et al. (2006). The calculations were performed for the same model parameters as in Fig. 6.

son for the modulation in X-rays seems to be adiabatic losses which should dominate over the radiative (synchrotron and IC) losses of electrons. We demonstrate that this assumption allows us to explain, at least qualitatively, the spectral and temporal characteristics of the combined *Suzaku* and HESS data. In particular, the introduction of adiabatic losses not only provides a natural explanation for the rather stable photon index of the X-ray spectrum  $\Gamma_X \simeq 1.5$ , but also allows one to approximately reproduce the TeV gamma-ray spectra.

The gamma-ray data require a location of the production region at the periphery of the binary system at  $d \sim 10^{12}$  cm. This constraint allows a quite robust estimate of the magnetic field of a few Gauss to be derived directly from the X/TeV flux ratio, and an adiabatic loss time of a few seconds to provide the dominance of adiabatic losses. In the case of a relativistically expanding source, the size of the production region should not exceed  $10^{11}$  cm. The adiabatic cooling cannot be shorter than several seconds, and correspondingly, the size of the production region cannot be much smaller than  $10^{11}$  cm, since otherwise the electrons could not be accelerated up to energies beyond 10 TeV, even assuming an extreme acceleration rate close to the fundamental limit determined by quantum electrodynamics. There is little doubt that future simultaneous observations of LS 5039 with the *Suzaku*, *Fermi*, and HESS telescopes will provide key information for understanding the nature of this mysterious non-thermal source.

T. Kishishita and T. Tanaka are supported by research fellowships of the Japan Society for the Promotion of Science for Young Scientists. The authors acknowledge support by the Spanish DGI of MEC under grant AYA2007-6803407171-C03-01, as well as partial support by the European Regional Development Fund (ERDF/FEDER). V.B.R. acknowledges support by the Spanish DGI of MEC under grant AYA2007-6803407171-C03-01, as well as partial support by the European Regional Development Fund (ERDF/FEDER).



## REFERENCES

- Acciari, V. A., et al. 2008, *ApJ*, 679, 1427  
Aharonian, F., et al. 2005, *Science*, 309, 746  
Aharonian, F. A., et al. 2005, *A&A*, 442, 1  
Aharonian, F., et al. 2006, *A&A*, 460, 743  
Albert, J., et al. 2006, *Science*, 312, 1771  
Albert, J., et al. 2007, *ApJ*, 665, L51  
Bogovalov, S. V., Khangulyan, D. V., Koldoba, A. V., Ustyugova, G. V., & Aharonian, F. A. 2008, *MNRAS*, 387, 63  
Bolton, C. T. 1972, *Nature*, 235, 271  
Bosch-Ramon, V., Paredes, J. M., Ribó, M. et al. 2005, *ApJ*, 628, 388  
Bosch-Ramon, V., et al. 2007, *A&A*, 473, 545  
Bosch-Ramon, V., Khangulyan, D., & Aharonian, F. A. 2008a, *A&A*, 482, 397  
Böttcher, M. 2007, *Astr. Phys.*, 27, 278  
Casares, J., et al. 2005, *MNRAS*, 364, 899  
Dubus, G. 2006, *A&A*, 456, 801  
Dubus, G., Cerutti, B., & Henri, G. 2008, *A&A*, 477, 691  
Fukazawa, Y., et al. 2008, *PASJ*, 61, S17  
Gruber, D. E., et al. 1999, *ApJ*, 520, 124  
Hillas, A. M. 1984, *ARA&A*, 22, 425  
Hoffmann, A. D., Klochkov, D., Santangelo, A., Horns, D., Segreto, A., Staubert, R., & Puehlhofer, G. 2009, *A&A*, 494, L37  
Johnston, S., et al. 1992, *ApJ*, 387, L37  
Khangulyan, D., & Aharonian, F. 2005, in *AIP Conf. Proc.*, 745, 359  
Khangulyan, D., Hnatic, S., Aharonian, F., & Bogovalov, S. 2007, *MNRAS*, 380, 320  
Khangulyan, D., Aharonian, F., & Bosch-Ramon, V. 2008a, *MNRAS*, 383, 467  
Khangulyan, D. V., Aharonian, F. A., Bogovalov, S. V., Koldoba, A. V., & Ustyugova, G. V. 2008b, *International Journal of Modern Physics D*, 17, 1909  
Kokubun, M., et al. 2007, *PASJ*, 59, SP1, 53  
Koyama, K., et al. 2007, *PASJ*, 59, SP1, 23  
Krivonos, R., et al. 2007, *A&A*, 463, 957  
Marshall, H. L., Canizares, C. R., & Schulz, N. S. 2002, *ApJ*, 564, 941  
Martocchia, A., Motch, C., and Negueruela, I. 2005, *A&A*, 430, 245  
Mitsuda, K., et al. 2007, *PASJ*, 59, SP1, 1  
Motch, C., Haberl, F., Dennerl, K., Pakull, M., & Janot-Pacheco, E. 1997, *A&A*, 323, 853  
Paredes, J. M., Martí, J., Ribó, M., & Massi, M. 2000, *Science*, 288, 2340  
Paredes, J. M., Ribó, M., Ros, E., Martí, J., & Massi, M. 2002, *A&A*, 393, L99  
Perucho, M. & Bosch-Ramon, V. 2008, *A&A*, 482, 917  
Ribó, M., Reig, P., Martí, J., and Paredes, J. M. 1999, *A&A*, 347, 51  
Serlemitsos, P. J., et al. 2007, *PASJ*, 59, SP1, 9  
Sierpowska-Bartosik & Torres, D. 2008, *Astroparticle Physics. Phys.* 30, 239  
Takahashi, T. et al. 2007, *PASJ*, 59, SP1, 35  
Zabalza, V., Paredes, J. M., Bosch-Ramon, V., 2008, *Int. Jour. Mod. Phys. D*, 17, 1867